Supplementary Information

Unravelling anion-dominated interfacial structure of hybrid solid electrolytes via ssNMR

Yuhang Li[a], *Likun Chen*[a], *Shengnan Zhang*[b], *Yubin Li*[a], *Junwei Liang*[a], *Yuetao Ma*[a], *Ke Yang*[a], *Zhuo Han*[a], *Guanyou Xiao*[a], *Longxiang Yu*[a], *Chenjie Lou*[a], *Yan-Bing He*[a], *Feiyu Kang*[a], *Ming Liu*[a*]

[a] Shenzhen All-Solid-State Lithium Battery Electrolyte Engineering Research Center, Institute of Materials Research (IMR), Tsinghua Shenzhen International Graduate School, Tsinghua University, Shenzhen 518055, P. R. China.

[b] Section Storage of Electrochemical Energy Radiation Science and Technology Faculty of Applied Sciences Delft University of Technology, Mekelweg 15, Delft 2629 JB, The Netherlands

*Corresponding author. E-mail: liuming@sz.tsinghua.edu.cn (M. Liu).

Experimental section

PEO-based electrolyte preparation

Li_6PS_5Cl (LPSC) was purchased from Ganfeng LiEnergy technology Co., Ltd. Poly(ethylene oxide) (PEO, M_w=600,000) came from Sigma-Aldrich. Lithium bis((trifluoromethyl)sulfonyl) azanide (LiTFSI), lithium perchlorate ($LiClO_4$), lithium difluoro (oxalato)borate (LiDFOB) and acetonitrile (electronic grade) were purchased from DodoChem technology Co., Ltd. The lithium tricyanomethanide (LiTCM) was purchased from TCI (Shanghai) Development Co., Ltd. The molecular sieve was used to remove trace water in the acetonitrile before use. The molecular sieve was purchased from Shanghai Aladdin Biochemical Technology Co., Ltd.

In a typical experiment, 0.576 g of PEO, 0.0786 g LPSC and 0.215 g of LiTFSI (EO:Li = 16:1) were added to 15 mL acetonitrile solution in an argon-filled glove box (H_2O < 0.01ppm, O_2 < 0.2 ppm) and stirred for 24 h. The homogeneous slurry was poured into a Teflon mold at room temperature for 24 h and further dried under vacuum for 48 h. As for other electrolytes with different lithium salts, the same mol of LiDFOB (0.108 g) or $LiClO_4$ (0.080 g) was added to electrolytes to replace LiTFSI and other steps for preparations remain the same. Various molar percentages of LiTCM were added to replace the LiTFSI.

Cells assembly and electrochemical characterization

The sulfur and N-methyl-2-pyrrolidone (NMP) and carbon nanotubes (CNTs) were purchased from Shanghai Aladdin Biochemical Technology Co., Ltd. The PVDF5130 binder (M_w = 1,200,000), Super P, coin cell components (CR2032, spacer: 15.8 × 1 mm, spring:

15.4 × 1.1 mm) and were purchased from Guangdong Canrd New Energy Technology Co., Ltd. Lithium foil came from China Energy Lithium Co., Ltd.

The melt diffusion method was used to prepare a carbon–sulfur (CNT@S) composite[1, 2]. The S (70 *wt.*%) and CNTs (30 *wt.*%) were milled to prepare homogeneous precursor mixture. The precursor mixture was further heated at 155 °C for 24 h to prepare CNT@S composite under Ar atmosphere. The homogeneous slurry was prepared by stirring mixture (CNT@S: Super P: PVDF5130 = 80 *wt.*%: 10 *wt.*%: 10 *wt.*%) over 6 h, which was coated onto carbon-coated Al foil and dried at 80 °C overnight. The obtained electrodes were dried at 100 °C overnight in a vacuum oven before using. The areal mass loading of sulfur in cathodic chips was ~0.5 mg cm^{-2}. CR2032 coin cells were assembled in an argon-filled glove box (H_2O < 0.01 ppm, O_2 < 0.2 ppm), which was also used for preparing electrolyte. The galvanostatic charge-discharge tests of Li||S were tested on a Land 2001A battery testing system and Neware battery cycler (CT-4008T-5V10mA-164, Shenzhen, China) at 60 ºC within a voltage window of 1.7-2.8 V (vs. Li^+/Li).

The electrochemical impedance spectroscopy (EIS) and cyclic voltammetry (CV) and the Tafel curves were conducted on a VMP3 multichannel electrochemical station (Bio Logic Science Instruments, France). The ionic conductivities of electrolyte were measured by EIS from 7 MHz to 100 mHz with a 20 mV AC oscillation. The CV measurements of Li||Cu was tested in a voltage range from −0.1-2.5 V at a scanning rate of 0.1 mV s^{-1}. The CV test of Li||S was performed in a voltage range from 1.7-2.8 V at a scanning rate from 0.02 to 0.1 mV s^{-1} at 60 °C. The ionic conductivities (σ) of electrolyte were calculated using the EIS results of stainless steel (SS)|electrolyte|SS coin cells according to the following equation (1):

$$\sigma = \frac{L}{RS} \tag{1}$$

where L is the thickness of HSE, R is the resistance and S is the area of the SS.

The activation energy (E_a) of HSE was calculated according to the Arrhenius formula which describes the relationship between temperature and ionic conductivity equation (2):

$$\sigma = A\exp\left(-\frac{E_a}{RT}\right) \tag{2}$$

where A is a pre-exponential factor, T is the absolute temperature and R is the universal gas constant.

Material Characterizations

The morphologies of samples were conducted on the field emission scanning electron microscope (FE-SEM, HITACH S4800, Japan). AFM system (Bruker Dimension Ico) was employed to observe Young's modulus. The three-dimensional distribution was collected by time-of-flight secondary ion mass spectrometry (ToF-SIMS, PHI nanoTOF II, 30 keV, 2 nA) in a 100 μm × 100 μm × 50 nm region. The quantitative Li concentration along the depth of the fully discharged cathodes was obtained by neutron depth profiling (NDP) using the CARR NDP system (CARRNDP) at the China Advanced Research Reactor (CARR).

Solid-state NMR measurements were conducted on a Bruker Avance NEO 400 wide-bore spectrometer ($B_0 = 9.4$ T), The frequencies of ^{1}H, ^{6}Li, ^{7}Li and ^{31}P were 400.00, 58.87, 155.46 and 161.92 MHz. The chemical shifts of ^{6,7}Li were referenced with respect to a 1 M LiCl solution (0 ppm), while the ^{31}P signals were referenced to $NH_4H_2PO_4$ (0.81 ppm). Magic angle spinning (MAS) experiments were performed on 3.2mm HXY MAS direct variable temperature (VT) probes at a spinning speed of 10 kHz. The direct polarization (DP) experiments of ^{7}Li and ^{6}Li were performed via onepulse sequences method with π/2 pulse lengths of 3.5 and 4.0 μs. The recycle delay were set longer than five times of spin-lattice relaxation time for each nucleus for all experiments. VT 2D ^{7}Li–^{7}Li EXSY measurements were performed using typical EXSY pulse sequence for the HSE samples at different mixing times from 298 – 328 K. The ^{6}Li CP MAS (^{1}H → ^{6}Li) experiments were performed with contact time of 4.0 ms. 2D ^{1}H–^{6}Li HETCOR measurements were performed with a CP contact time of 4.0 ms for electrolyte. Onepulse ^{31}P measurements were conducted with a π/2 pulse length of 2.5 μs. The ^{31}P CP MAS (^{1}H → ^{31}P) experiments were measured with contact time of 2.5 ms. 2D ^{1}H-^{31}P HETCOR measurements were measured with a contact time of 5.5 ms. For both CP MAS and HETCOR experiments, proton decoupling was performed during acquisition using the SPINAL-64 decoupling sequence. All spectra were simulated by using Bruker TOPSPIN and ssNake software.

Theoretical calculation methods

The first-principles calculations were conducting using the Vienna ab initio simulation package (VASP) based on density-functional theory (DFT) with the projector augmented wave (PAW) method[3-6]. The generalized gradient approximation (GGA-PBE) functional of Perdew-Burke-Ernzerhoff (PBE) was used to define the exchange-correlation interaction[7]. Spin calculations were adopted. A cutoff energy of 450 eV was applied to the plane-wave basis. Structural relaxation was attained using the conjugate gradient (CG) method, iterated until the total energy error was below 10^{-5} eV, and the force on each atom was less than 0.02 eV/Å. A 15 Å vacuum layer was added along the Z axis to avoid the periodical effect, the lattice parameter is 10.51Å×14.54Å×34.03Å.

The Brillouin zone was sampled using a 3 × 3 × 1 Monkhorst-Pack k-point grid. To optimize the minimum-energy path (MEP) for Li migration, the climbing image nudged elastic band (CINEB) method was employed to pinpoint the transition state, imposing a force convergence criterion on each atom of 0.05eV/Å[8]. The binding energy of lithium salts was calculated based on the following equation:

$$E_{binding} = E_{complex} - (E_{lithium-ion} + E_{anion}) \quad (3)$$

where $E_{complex}$, $E_{lithium-ion}$, and E_{anion} represents the energy of the lithium salt complex, Li^+ and anion[9, 10]. The binding energy was calculated using the Gaussian 16 package at B2PLYP/def2TZVP level[6]. All adsorption models were fully optimized using the geometry optimization convergence criteria, with thresholds of 4.5×10^{-4} a.u. for the maximum force, 3.0×10^{-4} a.u. for the RMS force, 1.8×10^{-3} a.u. for the maximum displacement, and 1.2×10^{-3} a.u. for the RMS displacement.

Supplementary Text S1: Quantification of interphases Li$^+$ exchange

Quantification of exchange between PEO and LPSC was performed by fitting the evolution of the exchange signal to a diffusion model. This approach utilizes the analytical solution to Fick's second law: $\frac{\partial m(\vec{r},\vec{t})}{\partial t} = \vec{\nabla} \cdot \{D(\vec{r}) m(\vec{r},\vec{t})\}$, where $m(\vec{r},\vec{t})$ is the magnetization of Li at position $\vec{r}$ and $\vec{t}$, and D is the Li$^+$ self-diffusion coefficient. By using the mathematical models of Schmidt-Rohr and co-workers for spin diffusion, and by assuming the overall diffusivity to be equal to the effective diffusion coefficient, the magnetization transfer of Li-ions in the Li_6PS_5Cl can be set equal to the initial magnetization minus the rate of magnetization in the PEO[2]. Assuming the Li6PS5Cl phase is embedded in an infinite PEO phase, the magnetization transfer from Li6PS5Cl into PEO can be described by the following analytical expression:

$$\mathrm{m}(t_{mix}) = 1 - \left\{\frac{m_0}{2}\sqrt{4Dt_{mix}}\left[ierfc\left(\frac{d}{\sqrt{4Dt_{mix}}}\right) + ierfc\left(\frac{-d}{\sqrt{4Dt_{mix}}}\right) - \frac{2}{\sqrt{\pi}}\right]\right\}^3 \qquad (1)$$

where $\mathrm{ierfc(x)} = 1/\sqrt{\pi}\,\exp(-x^2) - x[l - \mathrm{erf}\,(x)]$ and d is the Li$^+$ diffusion distance from Li_6PS_5Cl phase to PEO phase[11-13].

Supplementary Text S2: Quantification of ^{6}Li-ion exchange ratio (Relative Intensity)

The ^{6}Li metal with diameter of 15.6 mm is used for cycling. The current density of 0.05 mA cm^{-2} and 0.05 mAh cm^{-2} is used for activating the battery and 0.1 mA cm^{-2} and 0.1 mAh cm^{-2} for cycling at 60 °C. The ^{7}Li-ion inside electrolyte were replaced by ^{6}Li-ion, and the Li-conducting pathways were identified by examining the content of ^{6}Li-ion in components of cycled electrolyte. By simulating the integrated peaks for each component before and after cycling, the contributions to Li$^+$ transport are quantified on basis of ratios between the ^{6}Li peaks integration increase. The relative intensity of each component is quantified by the ratio of the integrated signal intensities:

$$\text{Relative intensity} = \frac{\text{Integrated signal intensity after cycling}}{\text{Integrated signal intensity before cycling}} \qquad (2)$$

Supplementary Text S3: Calculation Li^+ diffusion coefficient via CV test

The fitting line can be analyzed by Randles-Sevcik equation:

$$I_p = 2.69 \times 10^5 \cdot n^{\frac{3}{2}} \cdot A \cdot D^{\frac{1}{2}} \cdot C \cdot v^{\frac{1}{2}}$$

where I_p is the peak current, n is the number of electrons in sulfur redox reaction, A is the electrode area (cm^2), D is the Li^+ diffusion coefficient, C is the concentration, and v is the scan rate ($\mathrm{V\ s}^{-1}$). As the cell configuration is the same for all batteries, n, A and C are constants. Therefore, the slope k obtained from I_p *vs*. $v^{0.5}$ linear relationship is proportional to $D^{0.5}$. The ratio of k^2 for different samples is equal to the ratio of D for different samples[14].

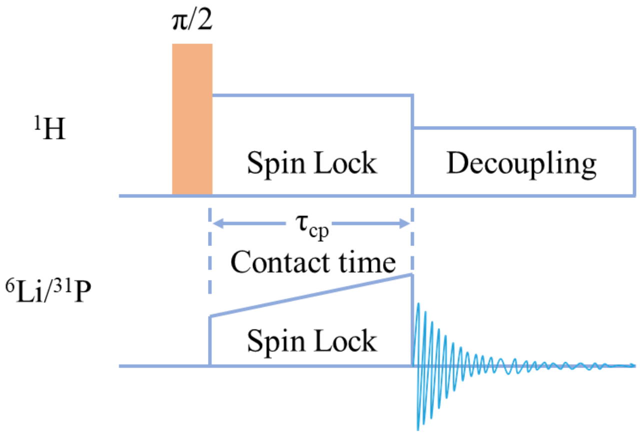

Figure S1. The phases of the proton CP pulse and excitation pulse are perpendicular to each other to spin-lock the magnetization.

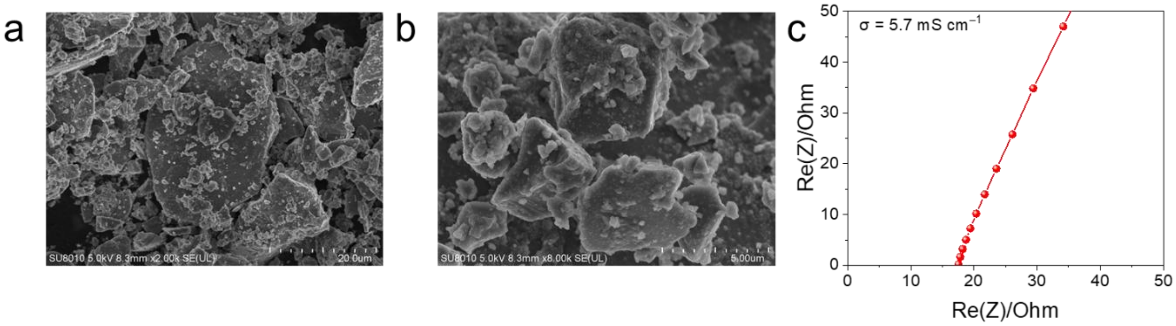

Figure S2. The morphology and ionic conductivity of LPSC. (a, b) SEM images of LPSC. (c) EIS spectrum of LPSC electrolyte.

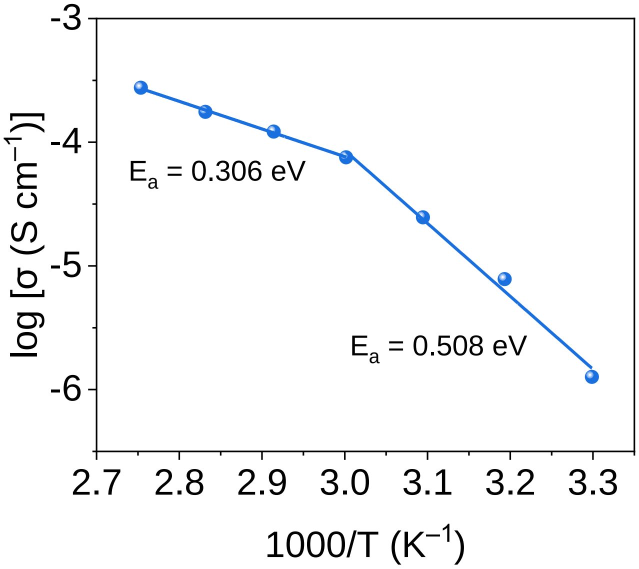

Figure S3. Arrhenius plot of the Li^+ conductivities at different temperatures for HSE-LiTFSI.

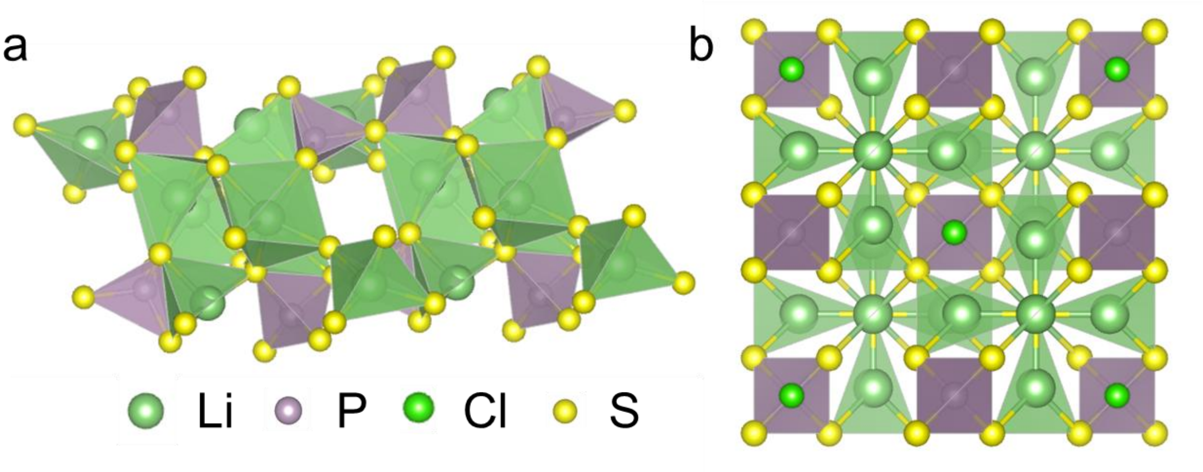

Figure S4. The crystal structure of $Li_4P_2S_7$ and LPSC for calculation.

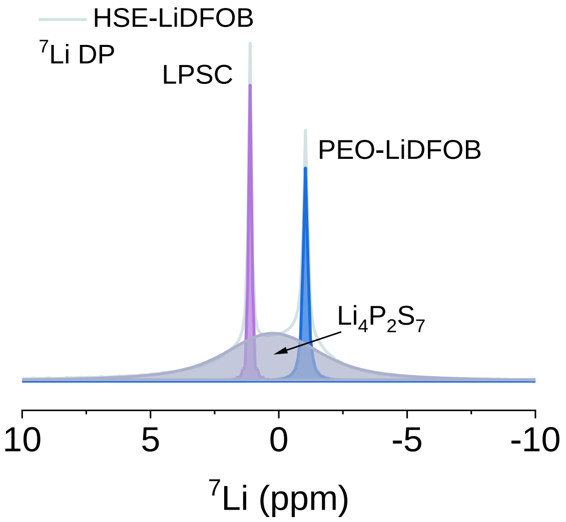

Figure S5. The ^{7}Li DP MAS spectrum of HSE-LiDFOB.

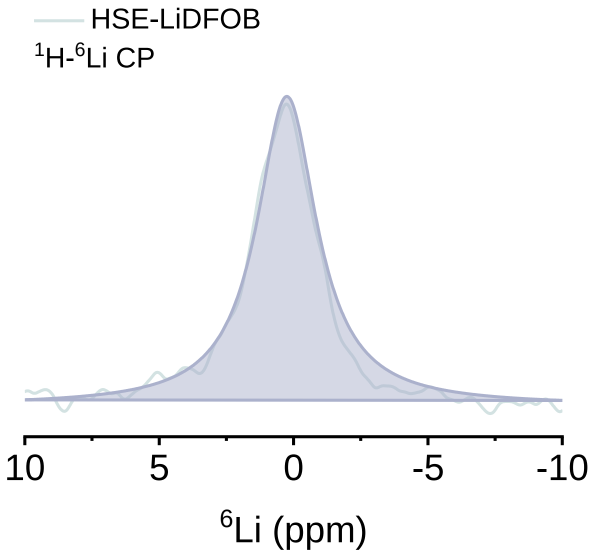

Figure S6. The ^{1}H-^{6}Li CP MAS spectrum of HSE-LiDFOB.

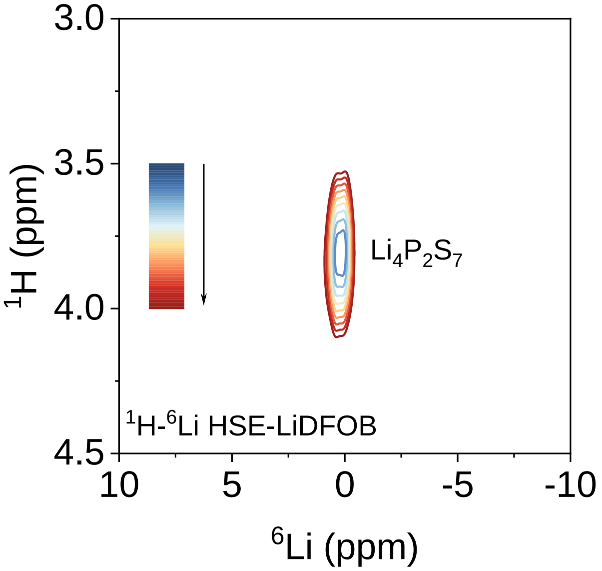

Figure S7. The ^{1}H-^{6}Li HETCOR of HSE-LiDFOB.

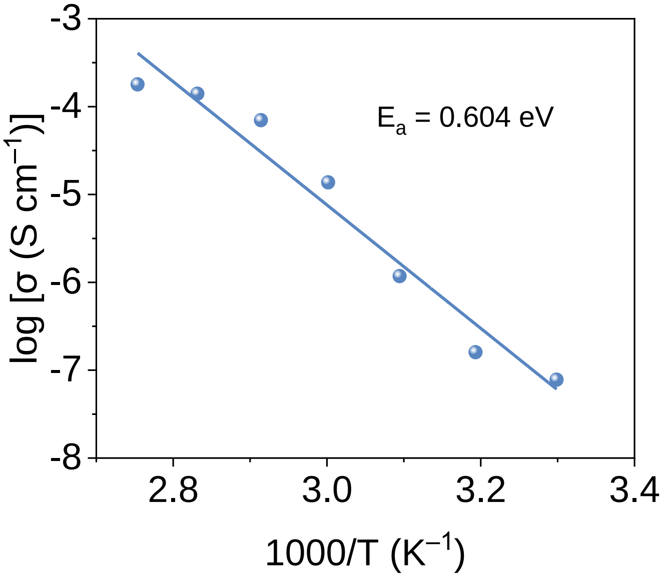

Figure S8. Arrhenius plot of the Li$^+$ conductivities at different temperatures for HSE-LiDFOB.

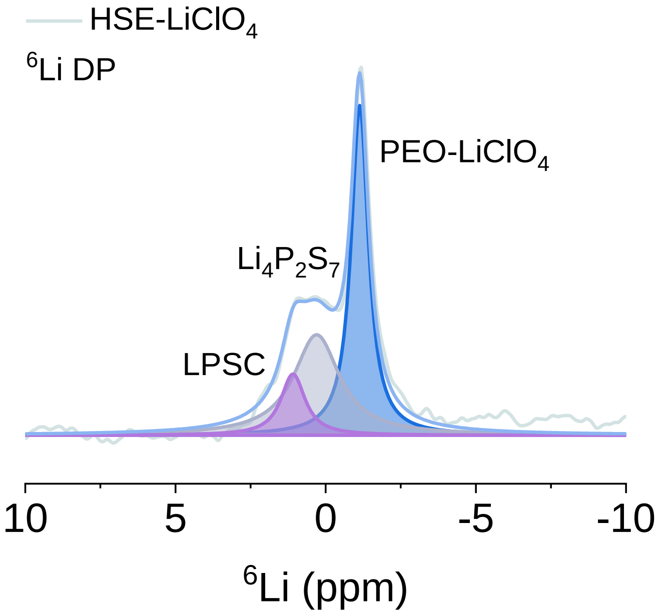

Figure S9. The ^{6}Li DP MAS spectrum of HSE-LiClO$_4$.

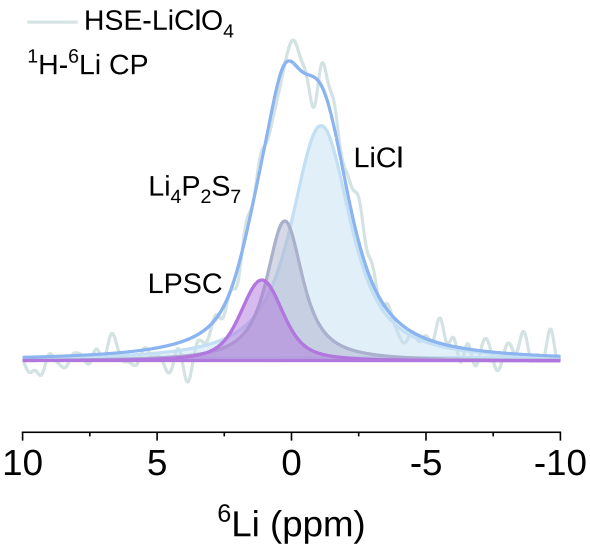

Figure S10. The ^1H-^6Li CP MAS spectrum of HSE-$LiClO_4$.

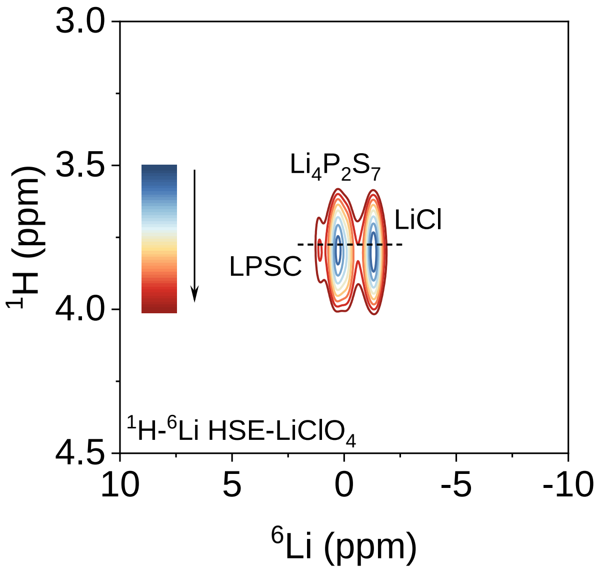

Figure S11.The ^{1}H-^{6}Li HETCOR spectrum of HSE-$LiClO_4$.

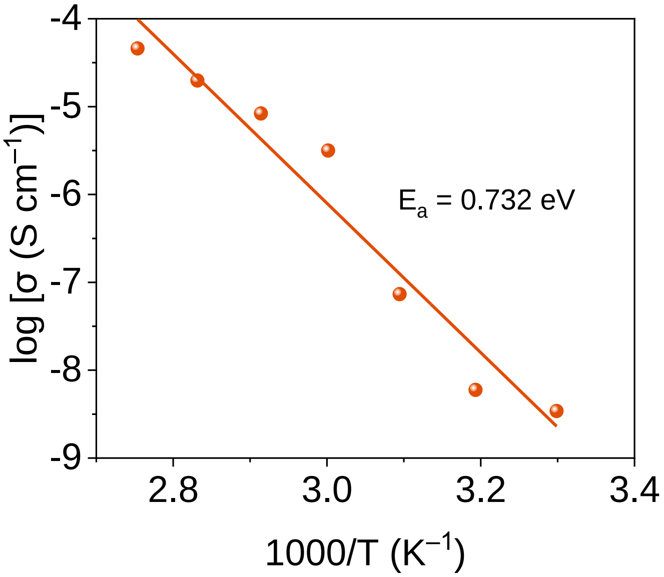

Figure S12. Arrhenius plot of the Li$^+$ conductivities at different temperatures for HSE-LiClO$_4$.

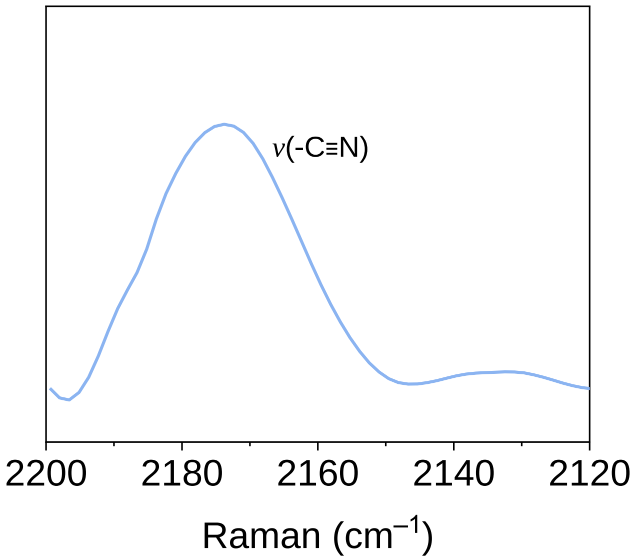

Figure S13. The Raman spectrum of HSE-LiTCM.

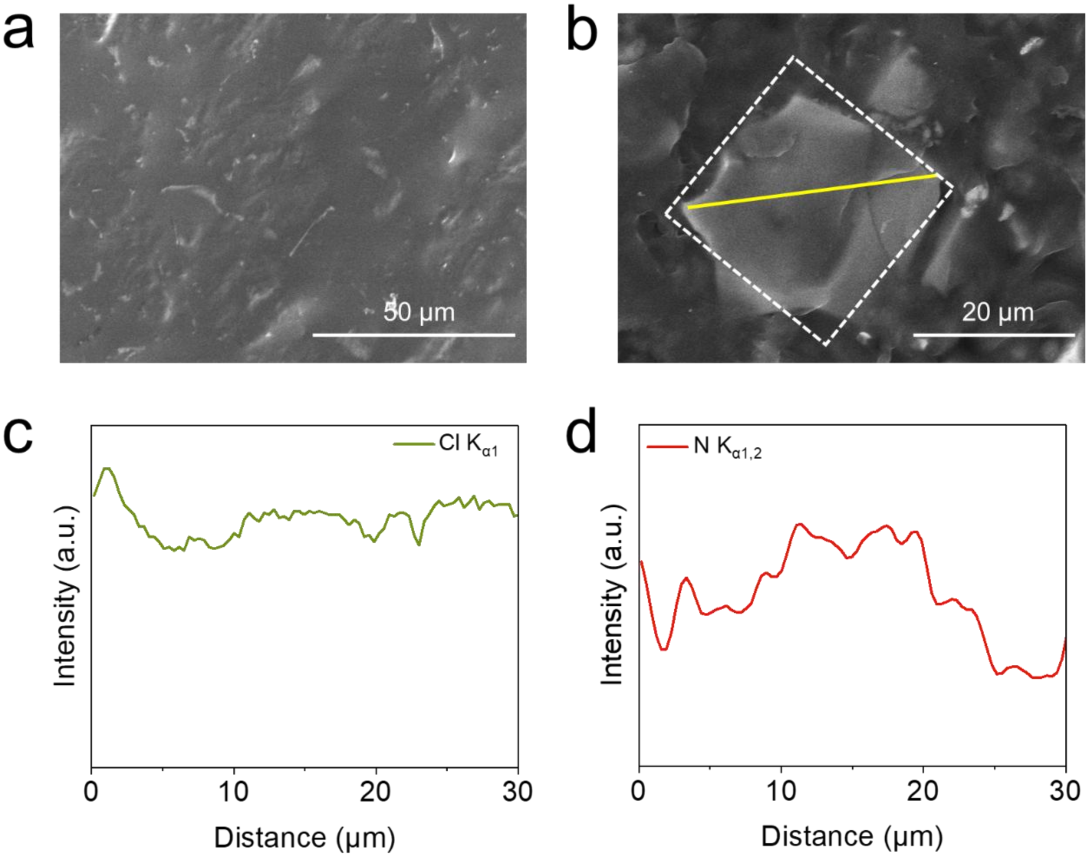

Figure S14. (a) The SEM image of HSE-LiTCM-100%, (b) selected region for EDS line scanning, the dashed box represents an LPSC particle. Line scans for (c) Cl $K_{\alpha1}$ and (d) N $K_{\alpha1,2}$.

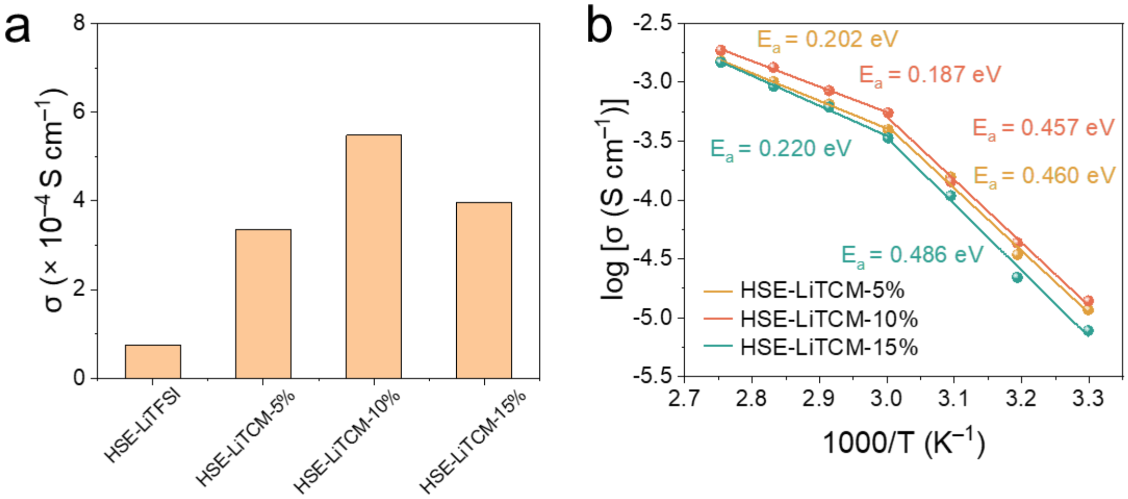

Figure S15. (a) Ionic conductivity and (b) Arrhenius plot of the Li^+ conductivities at different temperatures for HSE-LiTCM.

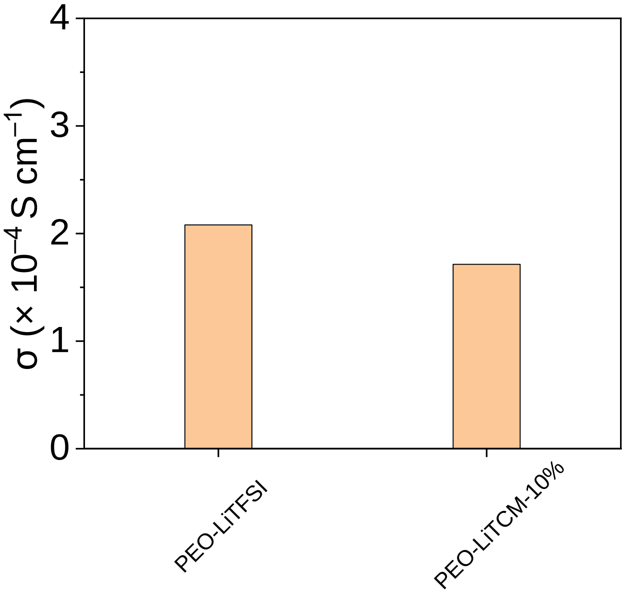

Figure S16. Ionic conductivity of PEO-LiTFSI and PEO-LiTCM-10% without addition of LPSC.

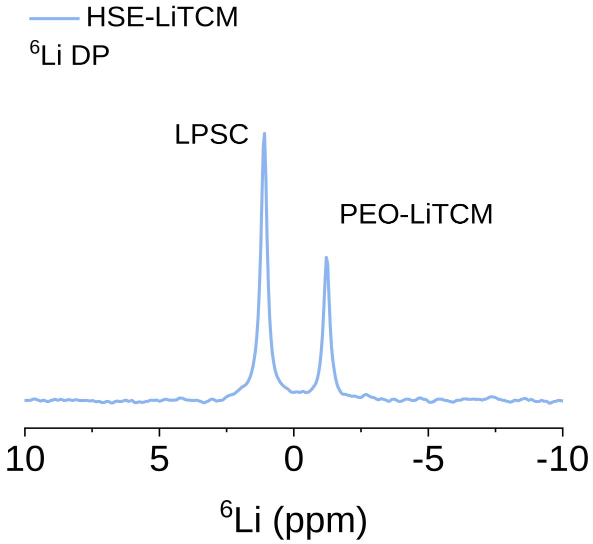

Figure S17.The ^{6}Li DP spectrum of HSE-LiTCM.

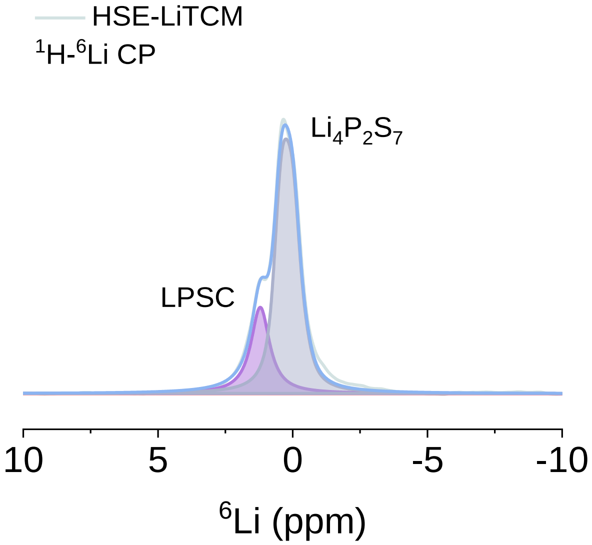

Figure S18. The ^{1}H-^{6}Li CP MAS spectrum of HSE-LiTCM.

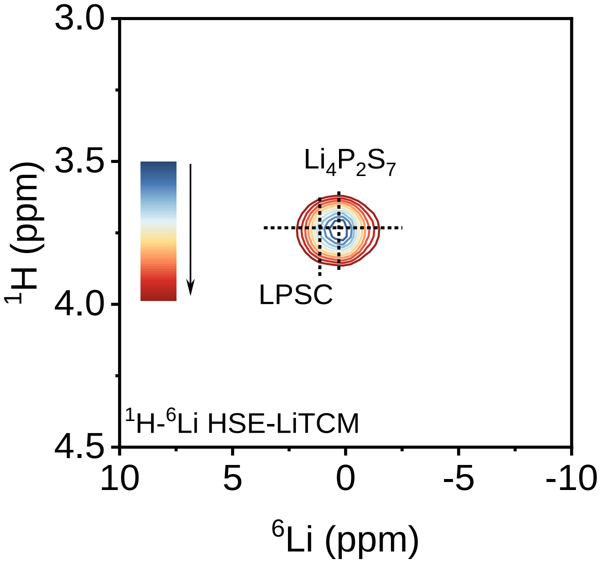

Figure S19. The ^{1}H-^{6}Li CP HETCOR spectrum of HSE-LiTCM.

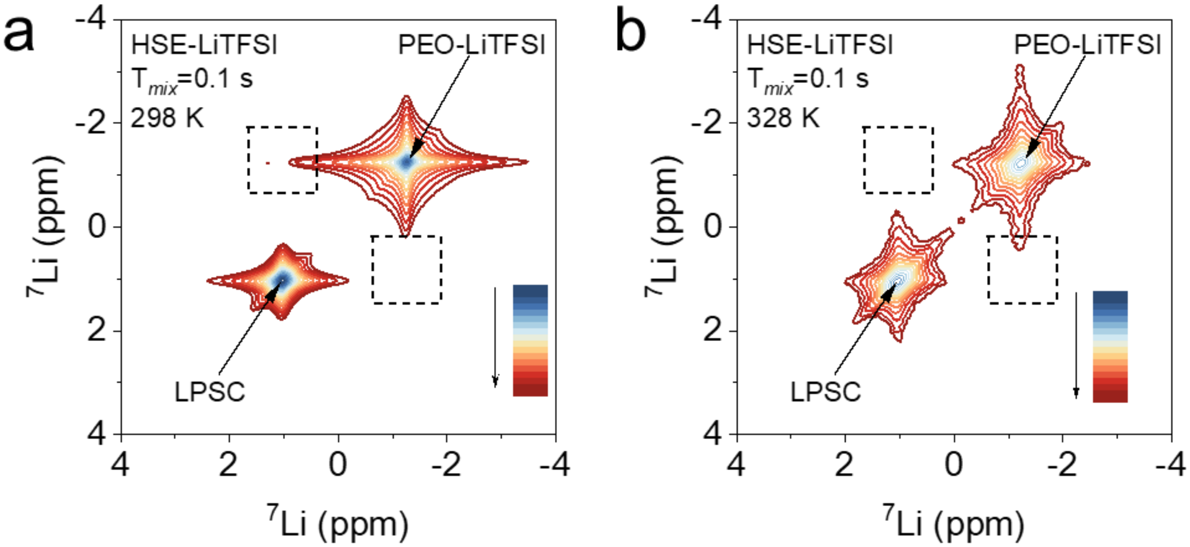

Figure S20. 2D ^{7}Li–^{7}Li EXSY spectrum of HSE-LiTFSI at mixing time of 0.1 s at (a) 298 K and (b) 328 K.

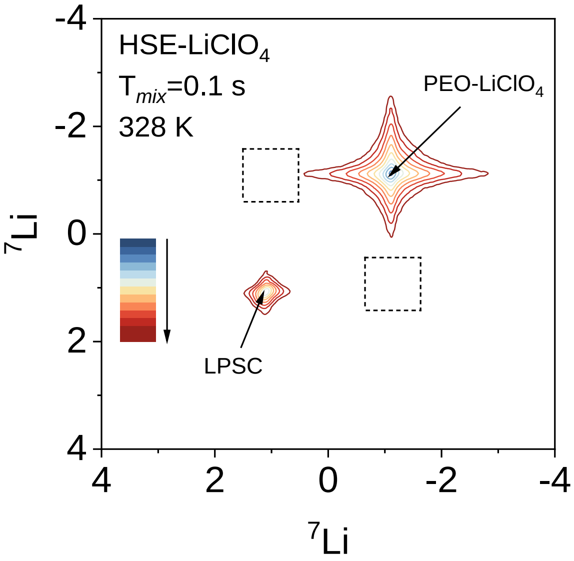

Figure S21. 2D ^{7}Li–^{7}Li EXSY spectrum of HSE-LiClO$_4$.

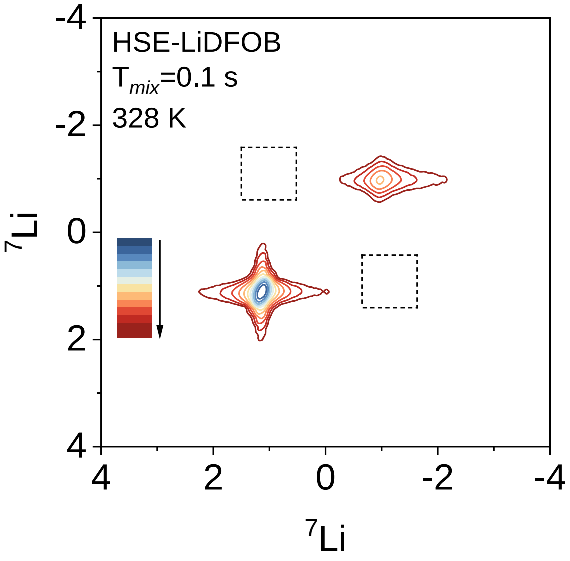

Figure S22. 2D ^{7}Li–^{7}Li EXSY spectrum of HSE-LiDFOB.

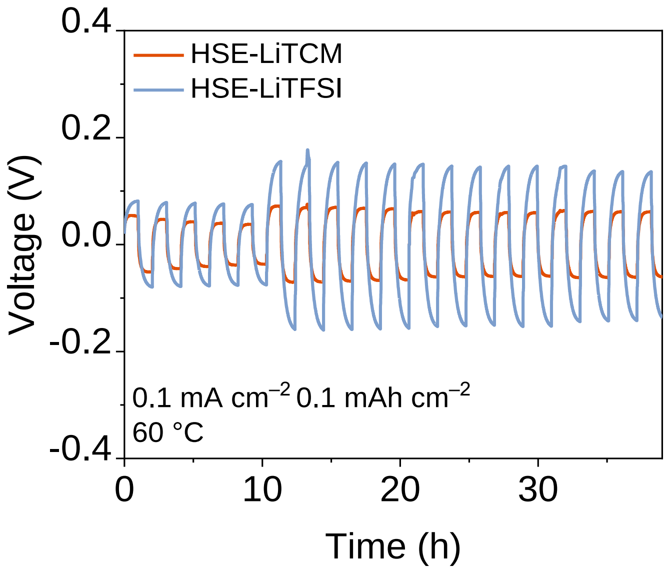

Figure S23. Electrochemical profile of the symmetric ^{6}Li|HSE|^{6}Li battery.

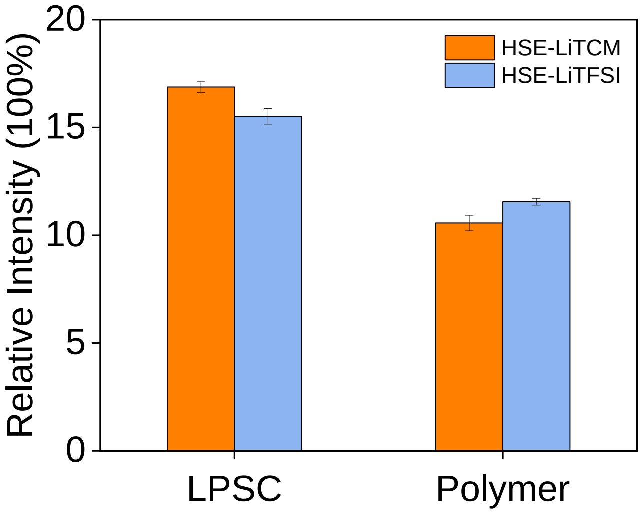

Figure S24. Quantified contributions to Li^+ transport of components in HSEs.

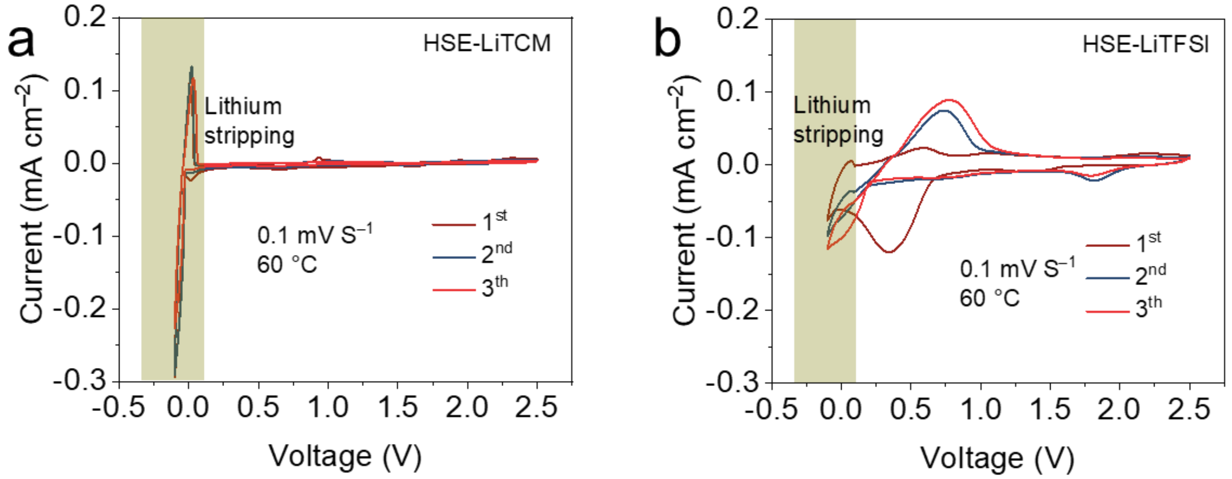

Figure S25. CV curves of Li-Cu batteries based on HSE-LiTFSI and HSE-LiTCM.

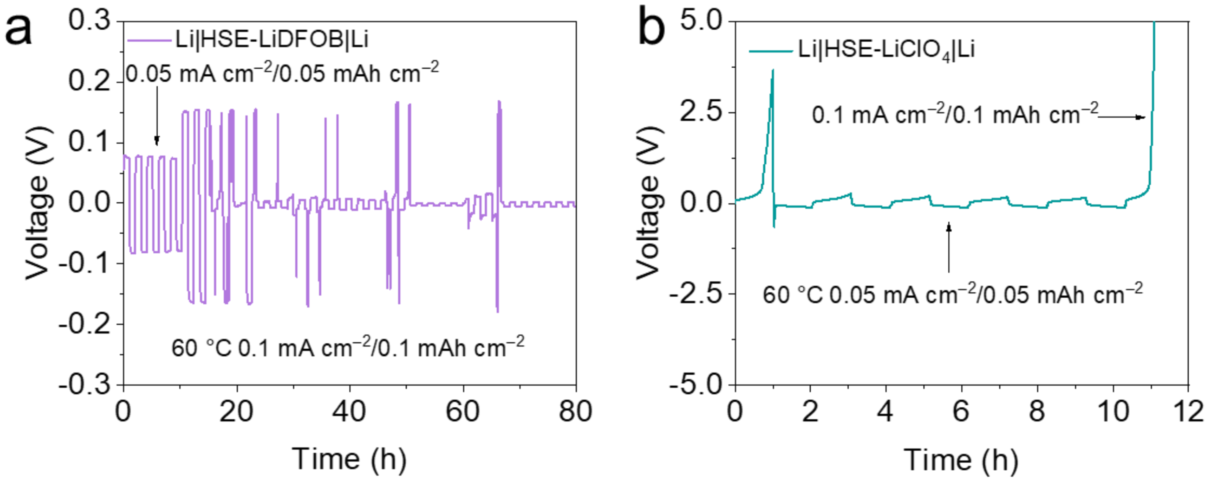

Figure S26. The cyclic stability test of Li||Li symmetric cells using (a) HSE-LiDFOB and (b) HSE-$LiClO_4$ at 0.1 mAcm^{-2} with 0.1 mAh cm^{-2}.

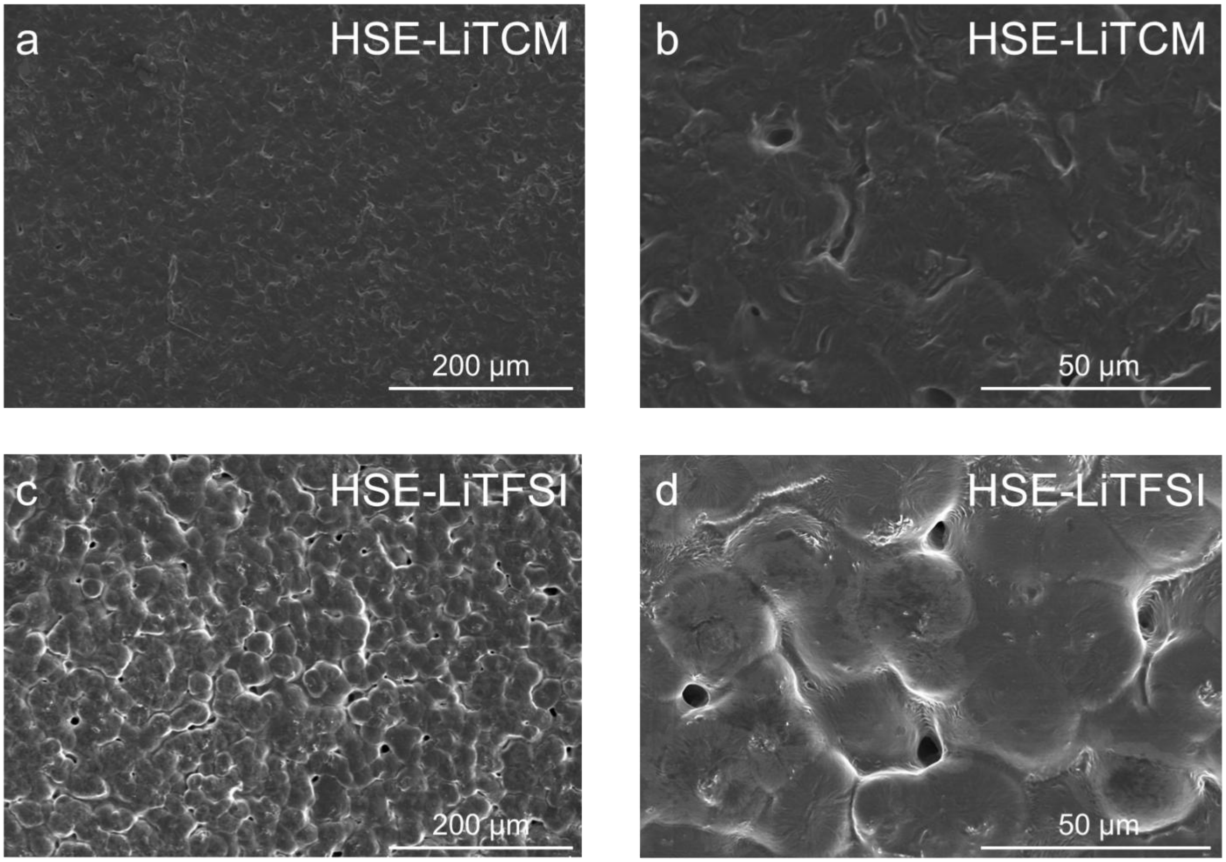

Figure S27. The surface SEM of (a, b) HSE-LiTCM and (c, d) HSE-LiTFSI.

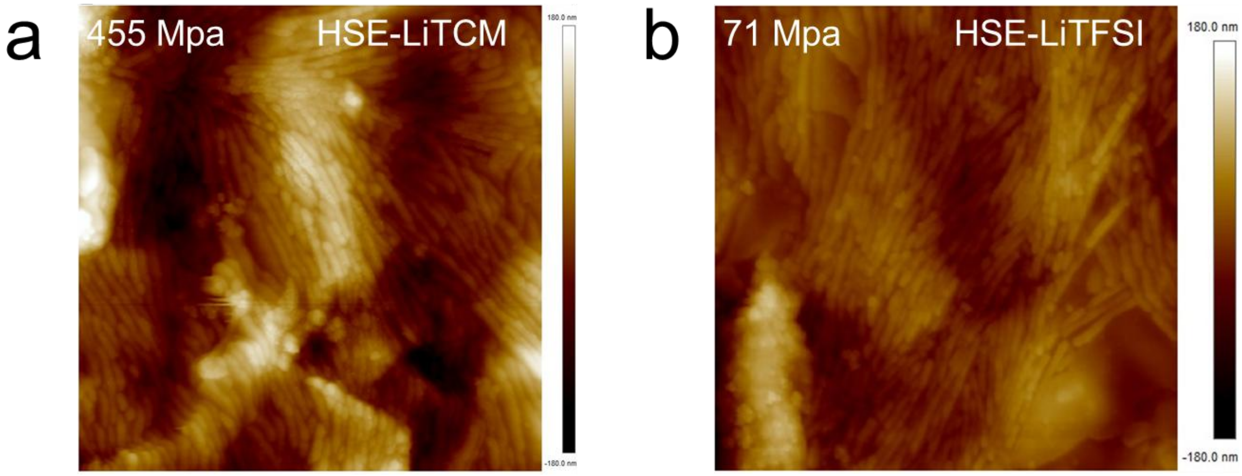

Figure S28. The AFM topography of (a) HSE-LiTCM and (b) HSE-LiTFSI.

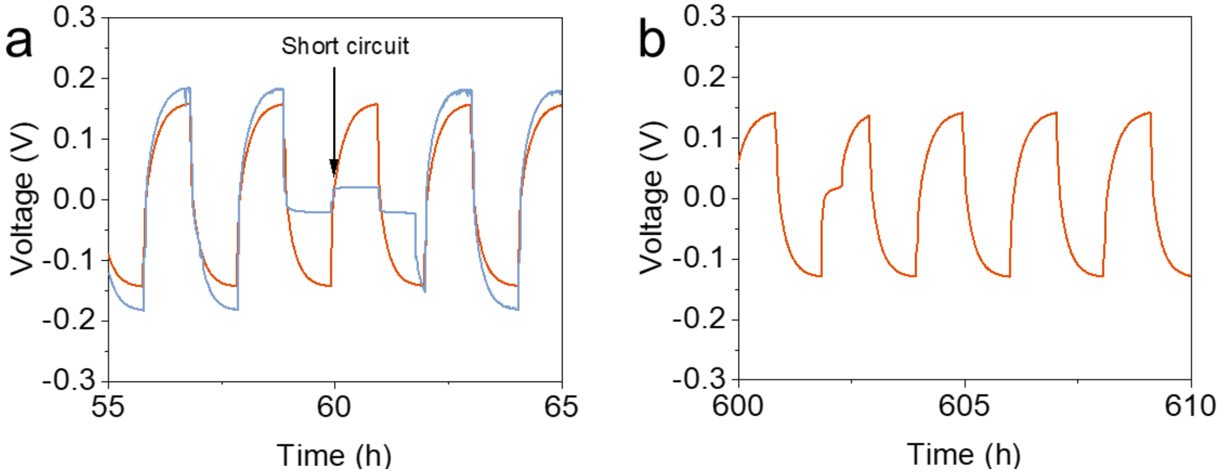

Figure S29. The cyclic stability test of Li||Li symmetric cells using HSE-LiTFSI and HSE-LiTCM at 0.2 mAcm^{-2} with 0.2 mAh cm^{-2}.

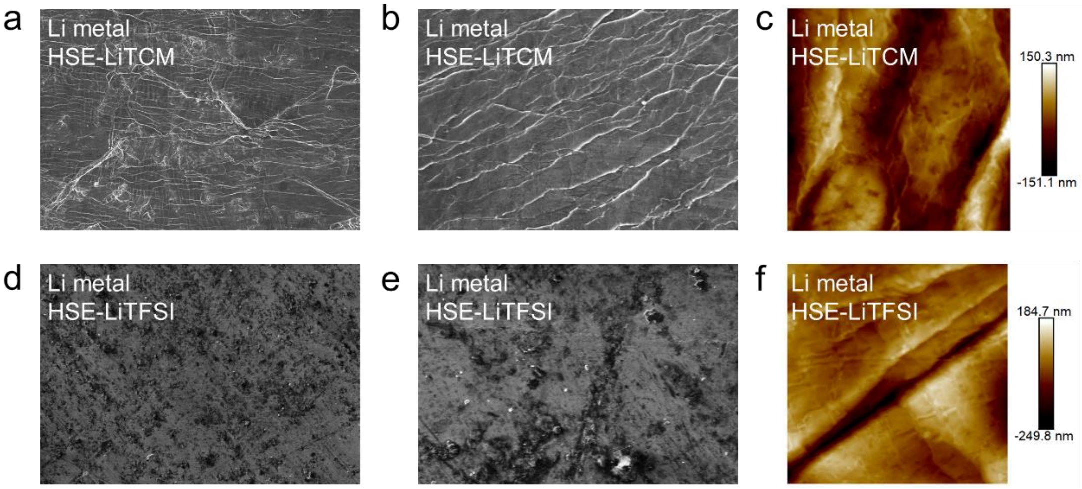

Figure S30. (a, b) SEM images and (c) the AFM image of the cycled Li anode in Li|HSE-LiTCM|Li; (d, e) SEM images and (f) the AFM image of the cycled Li anode in Li|HSE-LiTFSI|Li.

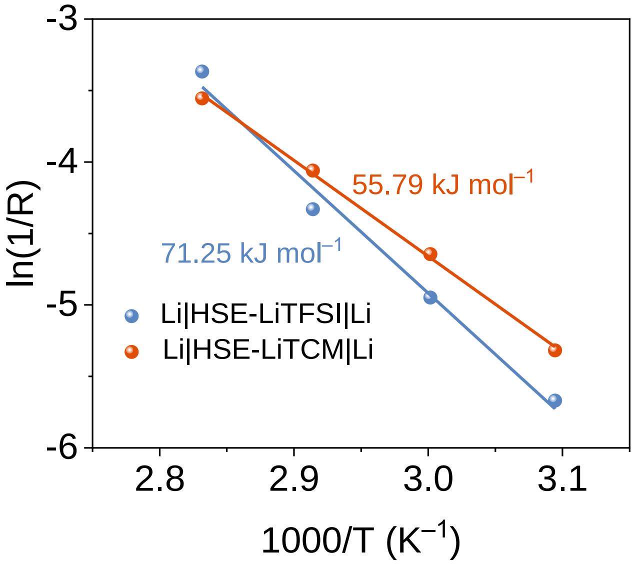

Figure S31. The activation energies of Li||Li symmetric cells using HSE-LiTFSI and HSE-LiTCM.

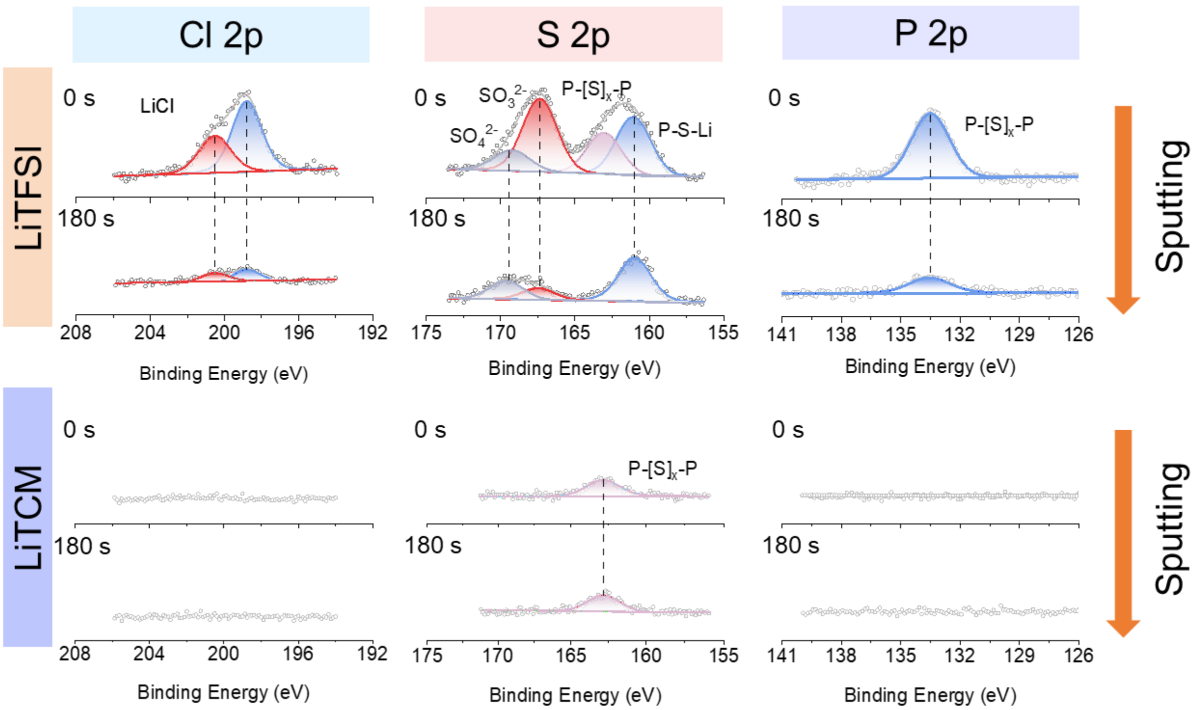

Figure S32. XPS spectra (Cl 2p, S 2p, P 2p) of SEI formed on the cycled Li anode in HSE-LiTFSI and HSE-LiTCM.

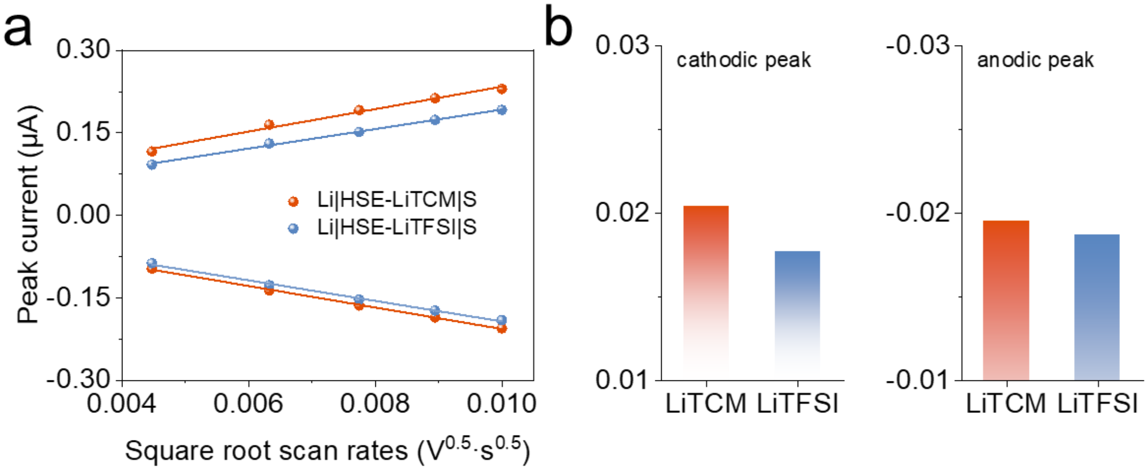

Figure S33. (a) The relationship between peak current and square root scan rate ($v^{0.5}$) of Li||S cells with HSE-LiTCM and HSE-LiTFSI. (b) Comparison of diffusion coefficients of Li^+ in sulfur electrodes using different electrolytes.

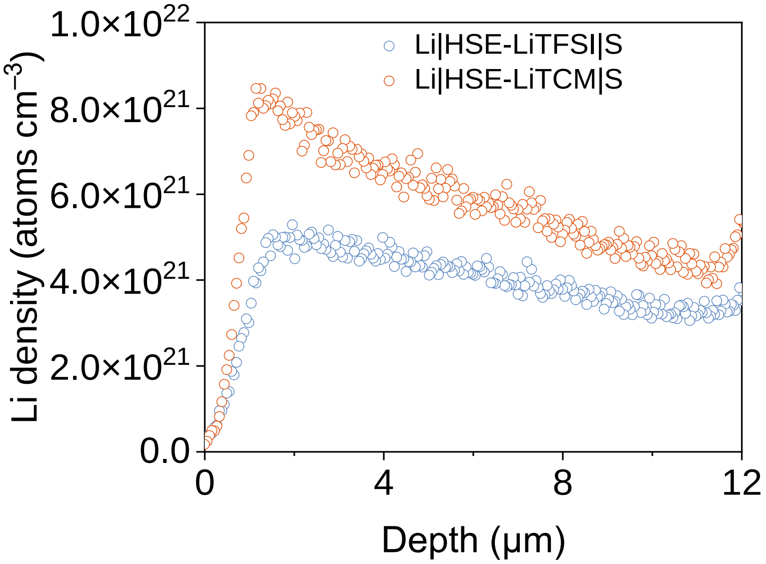

Figure S34. Li concentration curves of Li||S cells with HSE-LiTCM and HSE-LiTFSI electrolyte at 0.05C full discharge.

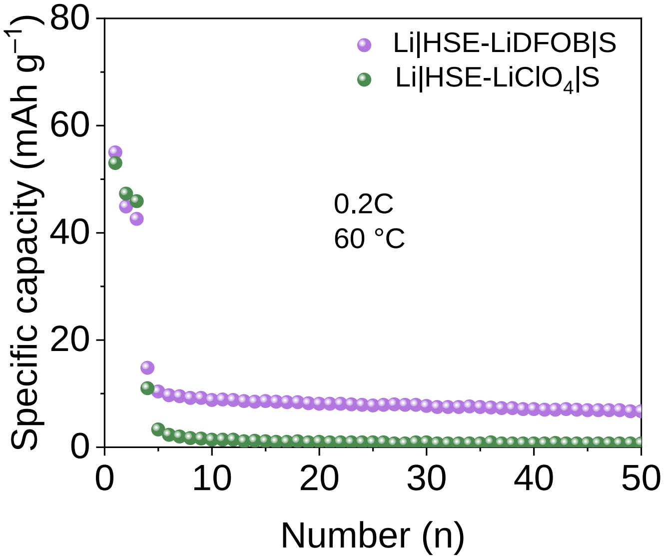

Figure S35. The Li||S full cells using HSE-LiDFOB and HSE-$LiClO_4$ at 0.2C.

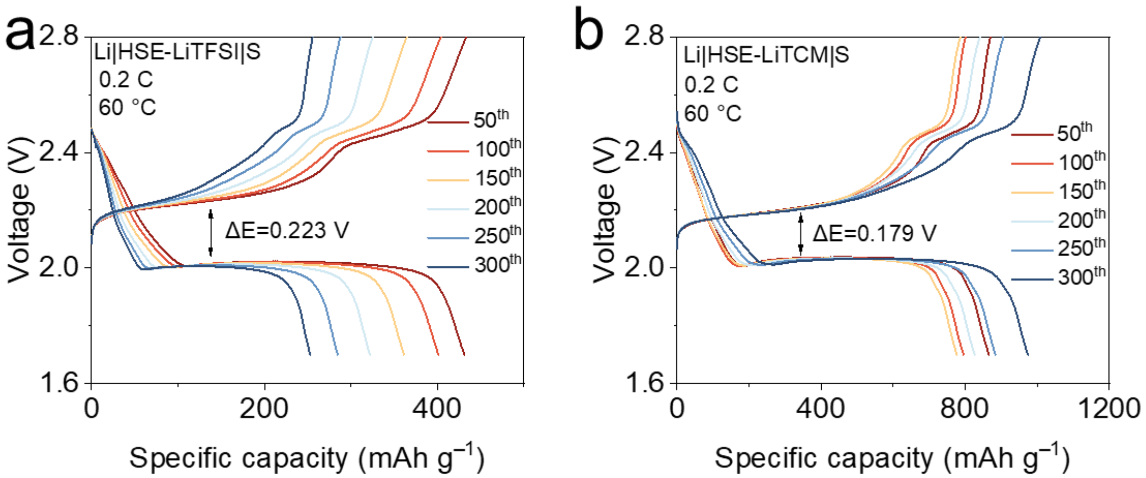

Figure S36. The charge-discharge curves of Li||S cells with HSE-LiTCM and HSE-LiTFSI.

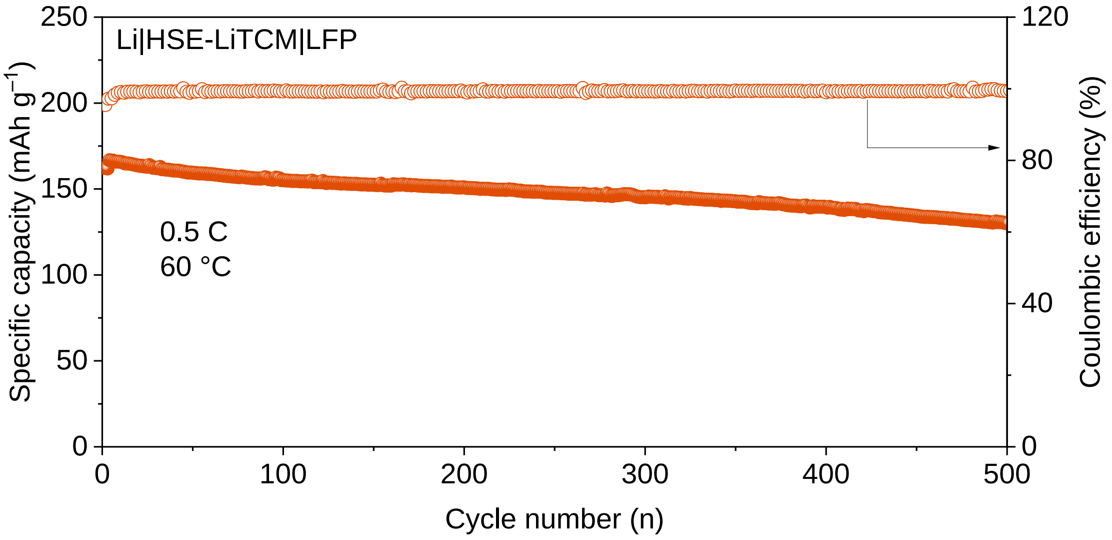

Figure S37. Long-term cycling stability of Li||LFP full cells with HSE-LiTCM.

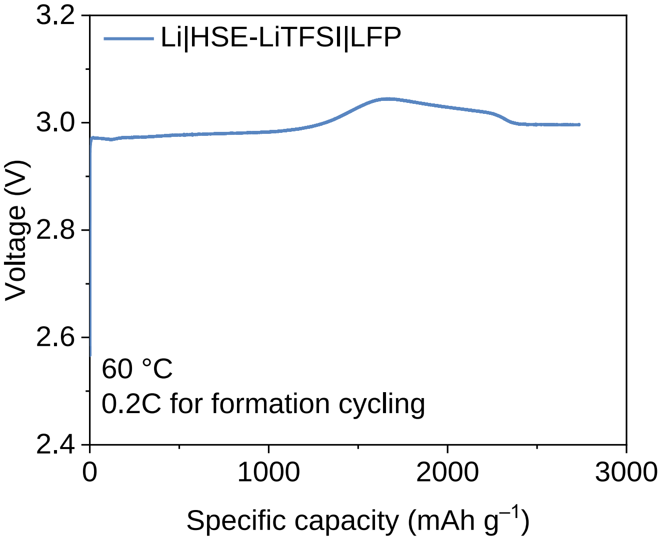

Figure S38. The charge-discharge curves of Li||LFP full cells with HSE-LiTFSI.

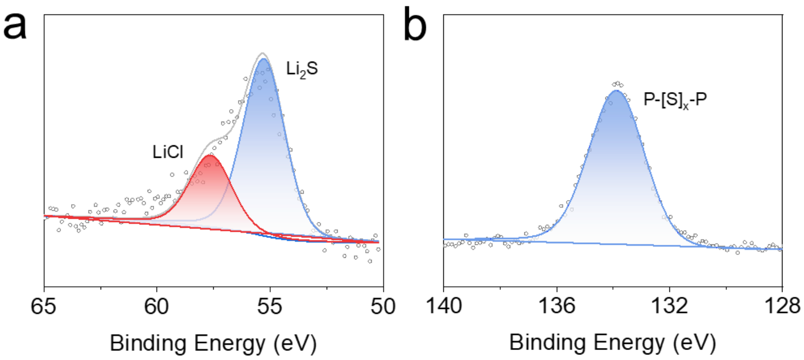

Figure S39. XPS spectra (Li 1s, P 2p) of the cycled LFP cathode using HSE-LiTFSI.

Table S1. Summary of solid-state lithium-sulfur batteries reported in the literature.

Electrolyte	**Rate (C)**	**Cycle**	**Decay (%)**	**Ref.**
PEO-LPSC-LiTCM	0.2	300	0.08	This work
PDOL	0.1666 mA g^{-1}	100	0.4	*Adv. Mater., 2023, 35, 2212039*
PDOL	0.2	200	0.18	*Angew. Chem. Int. Ed., 64, 2025, e202417105*
PEO-PAN	0.1	75	0.5	*Adv. Funct. Mater., 2022, 32, 2203272*
PVDF-HFP	0.2	100	0.32	*Energy Environ. Sci., 2022, 15, 4289-4300*
cellulose-Li_6PS_5Cl	0.1	100	0.16	*Adv. Funct. Mater., 2021,31, 2101985*
$Li_{10}GeP_2S_{12}$–Li_3PS_4	0.4 A g^{-1}	100	0.09	*Adv. Mater., 2019, 31, 1808100*
Li_3PS_4	0.2	100	0.25	*Adv. Funct. Mater., 2021, 31, 2004239*
PDOL/PEG–SiO_2	0.1	110	0.5	*Adv. Mater., 2022, 34, e2110333*
PEO–Al_2O_3	0.1	60	0.38	*Adv. Funct. Mater., 2022, 31, 2001812*
PVDF-HFP/UCPBA	0.5	180	0.44	*Proc. Natl. Acad. Sci., USA 2023, 120, e2300197120*
PEO–$Li_{10}GeP_2S_{12}$	0.1	50	1.15	*Adv. Funct. Mater., 2022, 30, 1910123*

REFERENCES

1. X. Ji, K. T. Lee and L. F. Nazar, *Nat. Mater.*, 2009, **8**, 500-506.
2. K. Schmidt-Rohr and H. W. Spiess, *Multidimensional solid-state NMR and polymers*, Academic Press, 1994.
3. G. Kresse and J. Furthmüller, *Phys. Rev. B*, 1996, **54**, 11169-11186.
4. G. Kresse and J. Hafner, *Phys. Rev. B*, 1994, **49**, 14251-14269.
5. P. E. Blöchl, *Phys. Rev. B*, 1994, **50**, 17953-17979.
6. M. J. h. w. g. c. Frisch, 2009.
7. J. P. Perdew, K. Burke and M. Ernzerhof, *Phys. Rev. Lett.*, 1996, **77**, 3865-3868.
8. G. Henkelman, B. P. Uberuaga and H. Jónsson, *J. Chem. Phys.*, 2000, **113**, 9901-9904.
9. T. Lu and F. Chen, 2012, **33**, 580-592.
10. J. Zhang and T. Lu, *PCCP*, 2021, **23**, 20323-20328.
11. M. Wagemaker, A. Kentgens and F. J. N. Mulder, 2002, **418**, 397-399.
12. C. Yu, S. Ganapathy, E. R. v. Eck, H. Wang, S. Basak, Z. Li and M. J. N. c. Wagemaker, 2017, **8**, 1086.
13. C. Yu, S. Ganapathy, N. J. J. de Klerk, I. Roslon, E. R. H. van Eck, A. P. M. Kentgens and M. Wagemaker, *J. Am. Chem. Soc.*, 2016, **138**, 11192-11201.
14. J. Zhao, J. Jing, W. Li, W. Chen, T. Chen, H. Zhong, Y. Wang and J. Fu, *Energy Storage Mater.*, 2023, **63**, 102991.